inorganics

MDPI

Article

The Synthesis and Crystal Structure of Six Quaternary Lithium-Alkaline Earth Metal Alumo-Silicides and Alumo-Germanides, $A_2LiAlTt_2$ (A = Mg, Ca, Sr, Ba; Tt = Si, Ge)

Paraskevi Kontomaris [1], Gregory M. Darone [1], Laura C. Paredes-Quevedo [2] and Svilen Bobev [3,*]

1 Charter School of Wilmington, Wilmington, DE 19807, USA; kontomaris.paraskevi@charterschool.org (P.K.); gdarone@udel.edu (G.M.D.)
2 Departamento de Química, Facultad de Ciencias, Universidad Nacional de Colombia-Bogotá, Carrera 30 No. 45-03, Bogotá 111321, Colombia; lcparedesq@unal.edu.co
3 Department of Chemistry and Biochemistry, University of Delaware, Newark, DE 19716, USA
* Correspondence: bobev@udel.edu; Tel.: +1-302-831-8720

Abstract: Reported are the synthesis and structural characterization of a series of quaternary lithium-alkaline earth metal alumo-silicides and alumo-germanides with the base formula $A_2LiAlTt_2$ (A = Ca, Sr, Ba; Tt = Si, Ge). To synthesize each compound, a mixture of the elements with the desired stoichiometric ratio was loaded into a niobium tube, arc welded shut, enclosed in a silica tube under vacuum, and heated in a tube furnace. Each sample was analyzed by powder and single-crystal X-ray diffraction, and the crystal structure of each compound was confirmed and refined from single-crystal X-ray diffraction data. The structures, despite the identical chemical formulae, are different, largely dependent on the nature of the alkaline earth metal. The differing cation determines the structure type—the calcium compounds are part of the TiNiSi family with the *Pnma* space group, the strontium compounds are isostructural with Na_2LiAlP_2 with the *Cmce* space group, and the barium compounds crystallize with the PbFCl structure type in the *P*4/*nmm* space group. The anion (silicon or germanium) only impacts the size of the unit cell, with the silicides having smaller unit cell volumes than the germanides.

Keywords: lithium; germanium; silicon; solid-state structures; synthesis; Zintl phases

Citation: Kontomaris, P.; Darone, G.M.; Paredes-Quevedo, L.C.; Bobev, S. The Synthesis and Crystal Structure of Six Quaternary Lithium-Alkaline Earth Metal Alumo-Silicides and Alumo-Germanides, $A_2LiAlTt_2$ (A = Mg, Ca, Sr, Ba; Tt = Si, Ge). *Inorganics* **2023**, *11*, 351. https://doi.org/10.3390/inorganics11090351

Academic Editors: W. Adam Phelan, Mariya Zhuravleva and Satya Kushwaha

Received: 1 August 2023
Revised: 16 August 2023
Accepted: 23 August 2023
Published: 26 August 2023

1. Introduction

With climate change becoming increasingly dominant, switching from fossil fuels to sustainable energy sources and reducing global inefficiencies are main priorities. Zintl phases typically contain electropositive cations (alkali, alkaline earth, or rare earth metals) and electronegative early p-block metals and semimetals from groups 13 to 15, which are the (poly)anions [1]. Given that many Zintl phases are intrinsic semiconductors, they could be the bases for materials with applications in solid-state energy conversion and/or storage [2–10], which further sustainability.

In recent years, the lithiation behavior of Si-, Ge-, and Sn-based clathrates, many of which can be viewed as Zintl phases [11], has become the subject of increased research interest [12–22]. The undertaken fundamental studies, either by us or by several other teams, have been carried out in the hopes of adapting the clathrates' desirable characteristics for prospective high-capacity Li-ion battery applications [23,24]. In particular, over the course of our work with the type-I clathrates $Ba_8Al_xSi_{46-x}$ and $Ba_8Al_xGe_{46-x}$ ($0 < x < 16$) [21,22], we observed the presence of some unknown phases as reaction byproducts. The latter were presumed to be new quaternary compounds with hitherto unknown structures and compositions. These observations were the motivation to create the following research plan for the summer internship; and so, the goal of this research was the rational synthesis of new Zintl phases comprising lithium and silicon or germanium. Hence, we set out to explore the *A*–Li–Al–*Tt* systems (*A* = Mg, Ca, Sr, Ba; *Tt* = Si, Ge) and our starting points were the equiatomic nominal compositions. The syntheses quickly yielded several new compounds in each respective system. Below, we detail the synthetic work that led to the identification of the title compounds, as well as describe their crystal structures. At the outset, we draw attention to the fact that the structures, despite their same general chemical formula, are different (Figure 1). Each compound's differing anion (silicon or germanium) impacts only the size of the unit cell, with the silicides having smaller unit cell volumes than the germanides. The nature of the alkaline earth metal appears to influence which structure forms, with the calcium compounds being analogs of the TiNiSi/SrMgSi family (orthorhombic *Pnma* space group, no. 62), the strontium compounds being a part of the Na_2LiAlP_2 structural family (orthorhombic *Cmce* space group, no. 64), and the barium compounds crystallizing with the PbFCl structure type in the tetragonal *P*4/*nmm* space group (no. 129). To this end, attempts at the synthesis of $Mg_2LiAlSi_2$ and $Mg_2LiAlGe_2$ failed (*Vide infra*).

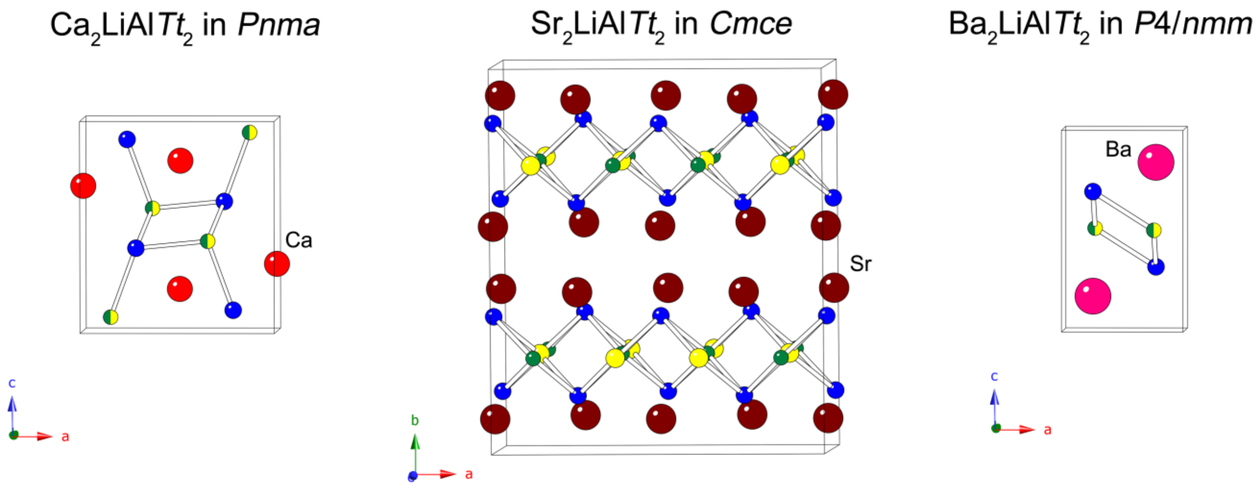

Figure 1. Schematic representation of the three types of crystal structures adopted by the $A_2LiAlTt_2$ (*A* = Ca, Sr, Ba; *Tt* = Si, Ge) compounds. Green, yellow, and blue colors represent the Al, Li, and *Tt* atoms, respectively; mixed-occupied Al/Li positions are shown as two-tone. Ca, Sr, and Ba atoms can be distinguished by the light red, dark red, and magenta spheres, respectively. Bonds (sticks) are drawn only between neighboring Al, Li, and *Tt* atoms. Unit cells are outlined.

Several europium and ytterbium compounds were also synthesized. The characterization work is still ongoing and the results will be detailed in a later publication. We will just note that the europium compounds appear to mirror the crystal chemistry of the barium compounds, but the ytterbium compounds have differing structures and compositions. For that reason, the synthesized rare earth metal compounds are not included here.

2. Results

Crystal data for $A_2LiAlTt_2$ (*A* = Ca, Sr, Ba; *Tt* = Si, Ge) can be found in Tables 1–3, respectively. We should note that our initial results from the system Ba–Li–Al–Ge, based on single-crystal X-ray diffraction work, showed the co-existence of Li and Al atoms on a single crystallographic site, which piqued our attention. Later on, the same result was replicated for the system Ba–Li–Al–Si. The Ca-compounds, although with a differing crystal structure, also showed Li and Al atoms on a single crystallographic site (Table 4). The refined chemical formulae in all four cases were $ALi_xAl_{1-x}Tt$ (*A* = Ca, Ba; *Tt* = Si, Ge) with $x \approx \frac{1}{2}$; however, subsequent synthetic work showed that changes in the nominal Li:Al ratio do not contribute to changes in the unit cell volume and there were no peak shifts when experimental and simulated powder X-ray diffraction patterns were compared. For the Sr-based compounds, Li and Al were found to occupy individual sites and were not disordered. Therefore, in this article, we labeled all six new alumo-silicides and alumo-germanides with the base formula $A_2LiAlTt_2$ (A = Ca, Sr, Ba; Tt = Si, Ge), neglecting the arguably small possibility of trivial deviations from the stated stoichiometry.

Table 1. Selected crystallographic data for $Ca_2LiAlSi_2$ and $Ca_2LiAlGe_2$ (T = 200(2) K; Mo $K\alpha$, λ = 0.71073 Å, space group $Pnma$ (no. 62)). Pearson symbol for this structure is $oP12$ [25].

Chemical Formula	$Ca_2LiAlSi_2$	$Ca_2LiAlGe_2$
Formula weight/g mol^{-1}	170.26	259.26
a/Å	7.2914 (7)	7.3255 (8)
b/Å	4.3411 (4)	4.3801 (5)
c/Å	7.9511 (8)	8.0246 (9)
V/Å^3	251.67 (4)	257.48 (5)
$\rho_{calc.}$/g cm^{-3}	2.25	3.34
$\mu_{(Mo\text{-}K\alpha)}$/cm^{-1}	27.3	136.5
Collected reflections	1999	5187
Independent reflections	430	450
Goodness-of-fit	1.074	1.044
R_1 ($I > 2\sigma_{(I)}$) [a]	0.0189	0.0287
wR_2 ($I > 2\sigma_{(I)}$) [a]	0.0407	0.0535
R_1 (all data) [a]	0.0233	0.0361
wR_2 (all data) [a]	0.0417	0.0553
$\Delta\rho_{max,min}$/e$^-$·Å^{-3}	0.38, −0.25	0.65, −0.76

[a] $R_1 = \sum||F_o| - |F_c||/\sum|F_o|$; $wR_2 = [\sum[w(F_o^2 - F_c^2)^2]/\sum[w(F_o^2)^2]]^{1/2}$, where $w = 1/[\sigma^2F_o^2 + (AP)^2 + (BP)]$ and $P = (F_o^2 + 2F_c^2)/3$; A and B are the respective weight coefficients (see the CIFs).

Table 2. Selected crystallographic data for $Sr_2LiAlSi_2$ and $Sr_2LiAlGe_2$ (T = 200(2) K; Mo $K\alpha$, λ = 0.71073 Å, space group $Cmce$ (no. 64)). Pearson symbol for this structure is $oS48$ [25].

Chemical Formula	$Sr_2LiAlSi_2$	$Sr_2LiAlGe_2$
Formula weight/g mol^{-1}	265.34	354.34
a/Å	12.5283 (4)	12.616 (3)
b/Å	14.4678 (7)	14.574 (3)
c/Å	6.2735 (7)	6.3133 (3)
V/Å^3	1137.1 (2)	1160.7 (4)
$\rho_{calc.}$/g cm^{-3}	3.10	4.06
$\mu_{(Mo\text{-}K\alpha)}$/cm^{-1}	191.7	285.3
Collected reflections	6957	4519
Independent reflections	908	848
Goodness-of-fit	1.18	1.10
R_1 ($I > 2\sigma_{(I)}$) [a]	0.0263	0.0334
wR_2 ($I > 2\sigma_{(I)}$) [a]	0.0434	0.0551
R_1 (all data) [a]	0.0388	0.0619
wR_2 (all data) [a]	0.0464	0.0617
$\Delta\rho_{max,min}$/e$^-$·Å^{-3}	1.28, −0.72	1.27, −0.94

[a] $R_1 = \sum||F_o| - |F_c||/\sum|F_o|$; $wR_2 = [\sum[w(F_o^2 - F_c^2)^2]/\sum[w(F_o^2)^2]]^{1/2}$, where $w = 1/[\sigma^2F_o^2 + (AP)^2 + (BP)]$ and $P = (F_o^2 + 2F_c^2)/3$; A and B are the respective weight coefficients (see the CIFs).

Table 3. Selected crystallographic data for $Ba_2LiAlSi_2$ and $Ba_2LiAlGe_2$ (T = 200(2) K; Mo $K\alpha$, λ = 0.71073 Å, space group $P4/nmm$ (no. 129)). Pearson symbol for this structure is $tP6$ [25].

Chemical Formula	$Ba_2LiAlSi_2$	$Ba_2LiAlGe_2$
Formula weight/g mol^{-1}	364.78	453.78
a/Å	4.5574 (6)	4.5965 (7)
c/Å	7.5582 (3)	7.5822 (7)
V/Å^3	156.98 (4)	160.19 (5)
$\rho_{calc.}$/g cm^{-3}	3.86	4.70

Table 3. *Cont.*

Chemical Formula	$Ba_2LiAlSi_2$	$Ba_2LiAlGe_2$
$\mu_{(Mo\text{-}K\alpha)}/cm^{-1}$	128.4	214.1
Collected reflections	1309	1316
Independent reflections	172	170
Goodness-of-fit	1.108	1.099
R_1 ($I > 2\sigma_{(I)}$) [a]	0.0167	0.0226
wR_2 ($I > 2\sigma_{(I)}$) [a]	0.0339	0.0443
R_1 (all data) [a]	0.0194	0.0286
wR_2 (all data) [a]	0.0348	0.0456
$\Delta\rho_{max,min}/e^{-}\cdot Å^{-3}$	1.10, −0.71	0.95, −0.91

[a] $R_1 = \sum||F_o| - |F_c||/\sum|F_o|$; $wR_2 = [\sum[w(F_o^2 - F_c^2)^2]/\sum[w(F_o^2)^2]]^{1/2}$, where $w = 1/[\sigma^2F_o^2 + (AP)^2 + (BP)]$ and $P = (F_o^2 + 2F_c^2)/3$; A and B are the respective weight coefficients (see the CIFs).

Table 4. Refined atomic coordinates for $A_2LiAlTt_2$ (A = Ca, Sr, Ba; Tt = Si, Ge). In all cases, unless noted otherwise, the atoms are refined anisotropically and the values of their equivalent isotropic displacement parameters ($U_{eq}/Å^2$) are given as well.

			$Ca_2LiAlSi_2$		
Atom	**Wyckoff Position**	x	y	z	$U_{eq}/Å^2$
Ca	4*c*	0.0100 (1)	1/4	0.6907 (1)	0.013 (1)
Li/Al [a]	4*c*	0.1500 (1)	1/4	0.0708 (1)	0.012 (1)
Si	4*c*	0.2802 (1)	1/4	0.3960 (1)	0.016 (1)
			$Ca_2LiAlGe_2$		
Ca	4*c*	0.0104 (1)	1/4	0.6923 (1)	0.014 (1)
Li/Al [a]	4*c*	0.1500 (1)	1/4	0.0704 (3)	0.018 (1)
Ge	4*c*	0.2780 (1)	1/4	0.3959 (1)	0.015 (1)
			$Sr_2LiAlSi_2$		
Sr1	8*e*	1/4	0.3349 (1)	1/4	0.009 (1)
Sr2	8*f*	0	0.1634 (1)	0.2283 (1)	0.010 (1)
Li	8*d*	0.1254 (7)	0	0	0.01 [b]
Al	8*d*	0.3720 (1)	0	0	0.012 (1)
Si1	8*e*	1/4	0.1028 (1)	1/4	0.009 (1)
Si2	8*f*	0	0.3968 (1)	0.2235 (2)	0.010 (1)
			$Sr_2LiAlGe_2$		
Sr1	8*e*	1/4	0.3352 (1)	1/4	0.010 (1)
Sr2	8*f*	0	0.1634 (1)	0.2294 (1)	0.011 (1)
Li	8*d*	0.1257 (5)	0	0	0.01 [b]
Al	8*d*	0.3726 (1)	0	0	0.015 (1)
Ge1	8*e*	1/4	0.1047 (1)	1/4	0.009 (1)
Ge2	8*f*	0	0.3951 (1)	0.2276 (1)	0.010 (1)
			$Ba_2LiAlSi_2$		
Ba	2*c*	1/4	1/4	0.6732 (1)	0.018 (1)
Li/Al [a]	2*a*	3/4	1/4	0	0.015 (1)
Si	2*c*	1/4	1/4	0.1914 (3)	0.020 (1)
			$Ba_2LiAlGe_2$		
Ba	2*c*	1/4	1/4	0.6743 (1)	0.016 (1)
Li/Al [a]	2*a*	3/4	1/4	0	0.016 (1)
Ge	2*c*	1/4	1/4	0.1953 (1)	0.018 (1)

[a] Refined occupancies were constrained to be Li:Al = 50:50. [b] Refined isotropically ($U_{eq} = U_{iso}$) and with value constrained to the average U_{eq} value for the heavy atoms in the structure.

As seen from Tables 1–3 (as well as from Table 4, where the atomic coordinates of each of the six structures are given), there are three basic structures adopted by each of the Ca, Sr, and Ba compounds, respectively. All three types of structures (Figure 1) share a common feature—tetrahedral (or rather distorted tetrahedral) coordination of Al and Li atoms by the atoms of the *Tt* element. In the case of the Ca and Ba compounds, there is no long-range ordering and the refined models have Li and Al atoms occupying the same crystallographic positions, while in the case of the Sr compounds, there is no randomization and the derived crystal structures of $Sr_2LiAlSi_2$ and $Sr_2LiAlGe_2$ are devoid of disorder. Apparently, the packing of the $AlTt_4$ and $LiTt_4$ fragments together with the increasing size of the alkaline earth metal atom (in the expected order Ca < Sr < Ba) governs the formation of each structure, as it will be discussed in the next section. In that regard, we will mention that we attempted to synthesize $Mg_2LiAlSi_2$ and $Mg_2LiAlGe_2$ using the same synthesis procedure (elements in the targeted stoichiometric ratio loaded into niobium tube, arc welded shut, enclosed in a silica tube under vacuum, and heated in tube furnaces according to the same heating profile as for the Ca, Sr, and Ba counterparts). The resultant products were not the quaternaries $Mg_2LiAlSi_2$ and $Mg_2LiAlGe_2$. Instead, three different crystals could be identified with a naked eye: (1) blue, shiny gem-like crystals; (2) atmosphere-reactive silver crystals; and (3) dark, hard, brittle crystals. The blue crystals were determined by single-crystal X-ray diffraction to be cubic Mg_2Si or Mg_2Ge [25]. The other crystals could not be identified reliably. We posit that Mg is either too small to form structures comparable to the Ca, Sr, and Ba compounds detailed in this paper, or may form covalent bonds with Al and the *Tt* element. Reactions with the heavier congener of Si and Ge, Sn, were not explored as a part of this study due to time limitations.

In summary, the reaction method detailed in this paper, with or without significant deviations, may produce more $A_2LiAlTt_2$ (A = Mg, Yb; Tt = Si, Ge, Sn) compounds, but further inquiries must be made.

3. Discussion

We begin the discussion with the structure of $Ca_2LiAlSi_2$ and $Ca_2LiAlGe_2$, which crystallize with the orthorhombic space group *Pnma* (no. 62). They are isotypic with TiNiSi structure type (Pearson symbol *oP*12) [25]; the structure has three unique positions in the asymmetric unit. As such, and as described previously, Li and Al atoms are considered to be statistically disordered.

A schematic representation of the structure is given in Figure 2. The chosen view shows that the structure can be viewed as a 3D network made up of edge- and corner-shared tetrahedra ($AlTt_4$ and $LiTt_4$), with the Ca atoms taking the space within the created channels. The tetrahedral units are slightly distorted from the ideal geometry and have two shorter and two longer Li/Al–*Tt* bonds. The respective distances are tabulated in Table 5.

Table 5. Selected interatomic distances (Å) in $Ca_2LiAlSi_2$ and $Ca_2LiAlGe_2$.

$Ca_2LiAlSi_2$		$Ca_2LiAlGe_2$	
Atom Pair	**Distance/Å**	**Atom Pair**	**Distance/Å**
Si—Li/Al	2.709 (1)	Ge—Li/Al	2.736 (3)
Si—Li/Al	2.754 (1)	Ge—Li/Al	2.776 (3)
Si—Li/Al × 2	2.6272 (6)	Ge—Li/Al × 2	2.653 (2)
Ca—Li/Al	3.190 (1)	Ca—Li/Al	3.201 (3)
Ca—Li/Al × 2	3.1093(7)	Ca—Li/Al × 2	3.130 (2)
Ca—Li/Al	3.349 (1)	Ca—Li/Al	3.381 (3)
Ca—Li/Al × 2	3.4301 (7)	Ca—Li/Al × 2	3.458 (2)
Ca—Si	3.0615 (7)	Ca—Ge	3.082 (1)
Ca—Si × 2	3.1089(5)	Ca—Ge × 2	3.1242 (7)
Ca—Si × 2	3.1168 (5)	Ca—Ge × 2	3.1414 (8)
Li/Al—Si × 2	2.6272 (6)	Li/Al—Ge × 2	2.653 (2)
Li/Al—Si	2.709 (1)	Li/Al—Ge	2.735 (3)
Li/Al—Si	2.754 (1)	Li/Al—Ge	2.776 (3)

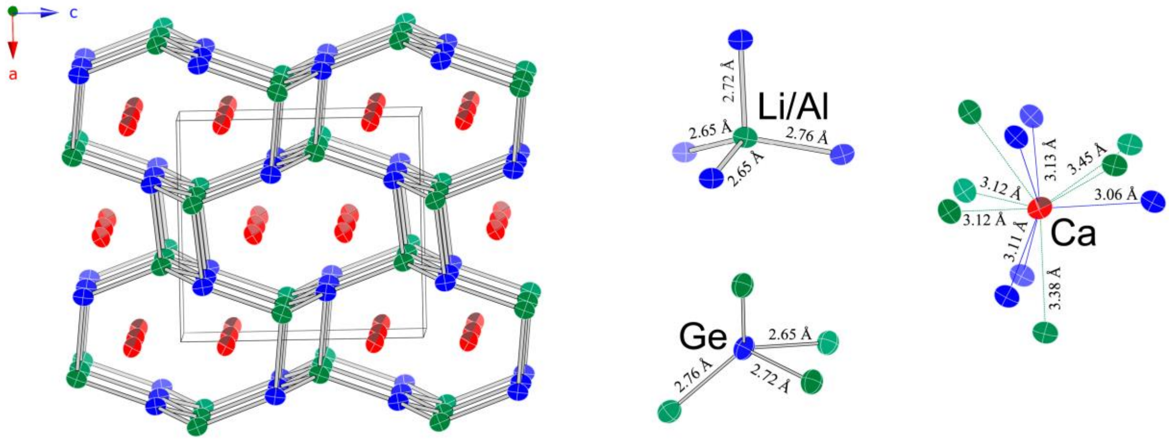

Figure 2. Schematic representation of the orthorhombic crystal structure of $Ca_2LiAlGe_2$ (TiNiSi/SrMgSi structure type, space group *Pnma*). Green, blue, and red colors represent Al/Li, Ge, and Ca atoms, respectively. Anisotropic displacement parameters are drawn at the 95% probability level. Unit cell is outlined. Distances (rounded to fewer significant figures) are indicated. A full list of all values with their standard deviations can be found in Table 5.

Four-fold coordination environments exist around the Si and Ge atoms too, but in that case, the distortions from the ideal tetrahedral angle, in particular, are more severe. Si—Li/Al and Ge—Li/Al distances are about 10% longer than the sum of the single-bonded Pauling covalent radii (r_{Li} = 1.225 Å; r_{Al} = 1.248 Å; r_{Si} = 1.173 Å; r_{Ge} = 1.242 Å) [26]. These distances match the reported values in a number of alumo-silicides and alumo-germanides, such as $Li_8Al_3Si_5$ [27,28], LiAlSi [28], $CaAl_2Si_2$ [29,30], $SrAl_2Si_2$ [31,32], $BaAl_2Si_2$ [33], $LnAl_2Si_2$ (*Ln* = Y, Sm, Tb, Dy, Yb) [34], $Ln_2Al_3Si_2$ and Ln_2AlSi_2 (*Ln* = Y, Tb-Lu) [35], $Ba_{7.5}Al_{13}Si_{29}$ [36], LiAlGe [37], $CaAl_2Ge_2$ [38,39], $LnAl_2Ge_2$ (*Ln* = Y, La, Nd, Gd, Tb, Lu) [40], $BaAl_2Ge_2$ [41], $A_3Al_2Ge_2$ (*A* = Ca, Sr, Ba) [42], and $LnAl_2X_2$ (*Ln* = Eu, Yb; *X* = Si, Ge) [43], among others. Ca atoms have a total coordination number 11, with 6 nearest Li/Al and 5 nearest *Tt* atoms. The shortest contact is $d_{Ca—Si}$ = 3.06 Å, which also fairly closely matches the sum of the single-bonded Pauling covalent radii of Si and Ca (r_{Ca} = 1.736 Å).

In the fully ionic approximation, the structures of $Ca_2LiAlSi_2$ and $Ca_2LiAlGe_2$ can be rationalized as $(Ca^{2+})_2(Li^+)(Al^{3+})(Si^{4-})_2$ and $(Ca^{2+})_2(Li^+)(Al^{3+})(Ge^{4-})_2$, i.e., the compounds should be considered intrinsic semiconductors. Applying the Zintl concept [1] also leads to the same conclusion—when treating Li as a cation and Al as a part of the polyanionic four-bonded substructure, it becomes possible to partition the valence electrons the following way: $(Ca^{2+})_2(Li^+)(4b\text{-}Al^{1-})(4b\text{-}Si^0)(0b\text{-}Si^{4-})$ and $(Ca^{2+})_2(Li^+)(4b\text{-}Al^{1-})(4b\text{-}Ge^0)(0b\text{-}Ge^{4-})$. To arrive at this formula breakdown, we are assuming covalent Si—Al and Ge—Al interactions; Si and Al are coordinated to Al atoms 50% of the time. In the remaining 50% of the time, Li takes the Al position and covalency of the Si—Li and Ge—Li is neglected, i.e., Si and Ge are treated as isolated, closed-shell anions.

Following periodic trends, the structure of $Sr_2LiAlSi_2$ and $Sr_2LiAlGe_2$ will be discussed next. These compounds are also orthorhombic, but with the base-centered space group *Cmce* (no. 64). They are isotypic with Na_2LiAlP_2 (Pearson symbol *oS*48) [44]. The structure has six unique positions in the asymmetric unit—two for the Sr atom, two for the Si or Ge atoms, and one each for the Li and Al atoms, Table 4. As such, and as described previously, this is the only "true 2-1-1-2" structure, given that Li and Al atoms are ordered crystallographically here.

A schematic representation of the structure is given in Figure 3. The chosen view shows that the structure can be viewed as slabs made up of all edge-shared $AlTt_4$ and $LiTt_4$ tetrahedra parallel to the *ac* plane. The general topology of the 2D polyanionic substructure is reminiscent of the PbO-like layers that are frequently observed in the structures of many pnictides and chalcogenides [45–47], and analogous to the layers seen in the tetragonal structures of $Ba_2LiAlSi_2$ and $Ba_2LiAlGe_2$, which will be discussed next. The difference is that here, given that there is no Li/Al disorder, the exact positions of Li and Al atoms are known and the ordering pattern is checkerboard-like, with a repeating sequence of AlTt_4 × 2 by LiTt_4 × 2 (Figure 3, right panel).

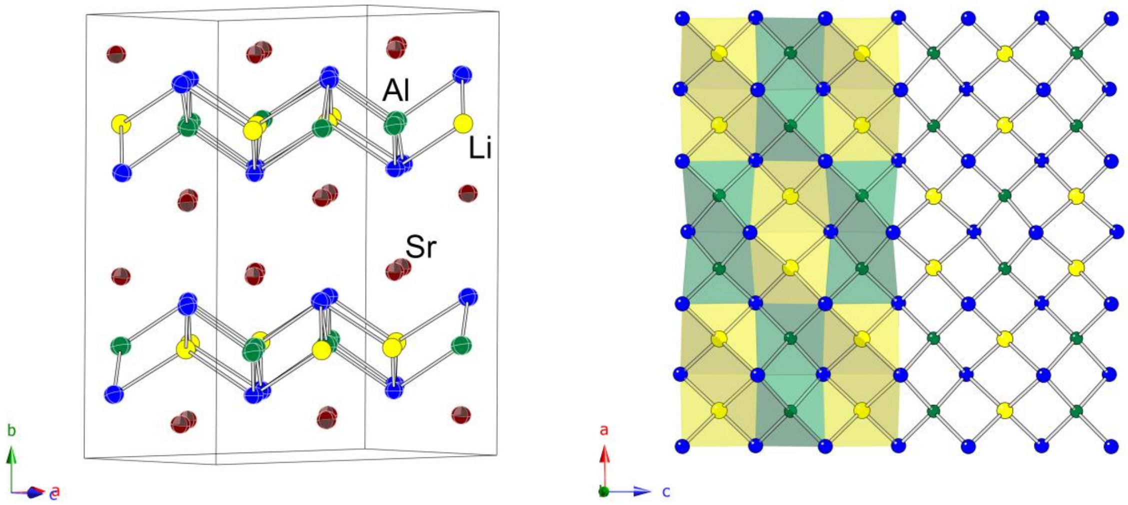

Figure 3. (**left**) Schematic representation of the orthorhombic crystal structure of $Sr_2LiAlGe_2$ (Na_2LiAlP_2 structure type, space group *Cmce*). The chosen projection is to highlight the similarity to another structure, and the unit cell is outlined. Green, yellow, blue, and red colors represent the Al, Li, Ge, and Sr atoms, respectively. Anisotropic displacement parameters are drawn at the 95% probability level. (**right**) A projection of a single [$LiAlGe_2$] slab, viewed down the *b*-axis. The checkerboard-like pattern of all edge-shared tetrahedra is emphasized.

The AlTt_4 and LiTt_4 tetrahedral units are ever so slightly distorted from the ideal geometry and have two shorter and two longer Li/Al–*Tt* bonds. The refined bond lengths match the sum of the single-bonded Pauling covalent radii of the elements well. Sr atoms are arranged in double layers between the [$LiAlSi_2$] and [$LiAlGe_2$] slabs. They have a total coordination number of nine, with five nearest *Tt* atoms, two nearest Al, and two neighboring Li atoms. All respective distances are tabulated in Table 6.

Table 6. Selected interatomic distances (Å) in $Sr_2LiAlSi_2$ and $Sr_2LiAlGe_2$.

$Sr_2LiAlSi_2$		**$Sr_2LiAlGe_2$**	
Atom Pair	**Distance/Å**	**Atom Pair**	**Distance/Å**
Si1—Al × 2	2.647 (1)	Ge1—Al × 2	2.686 (2)
Si1—Li × 2	2.666 (5)	Ge1—Li × 2	2.70 (1)
Si2—Al × 2	2.600 (1)	Ge2—Al × 2	2.643 (2)
Si2—Li × 2	2.775 (5)	Ge2—Li × 2	2.79 (1)
Sr1—Al × 2	3.2413 (9)	Sr1—Al × 2	3.264 (2)
Sr1—Li × 2	3.257 (4)	Sr1—Li × 2	3.275 (9)
Sr1—Si1 × 2	3.2639 (5)	Sr1—Ge1 × 2	3.2758 (7)
Sr1—Si1	3.358 (2)	Sr1—Ge2	3.360 (2)
Sr1—Si2 × 2	3.2621 (5)	Sr1—Ge2 × 2	3.2756 (7)
Sr2—Al × 2	3.3260 (9)	Sr2—Al × 2	3.343 (2)
Sr2—Li × 2	3.179 (5)	Sr2—Li × 2	3.206 (9)
Sr2—Si1 × 2	3.2554 (5)	Sr2—Ge1 × 2	3.2706 (7)
Sr2—Si2	3.226 (1)	Sr2—Ge2	3.2585 (6)
Sr2—Si2	3.285 (1)	Sr2—Ge2	3.281 (1)
Sr2—Si2	3.378 (2)	Sr2—Ge2	3.377 (2)
Al—Si1 × 2	2.647 (1)	Al—Ge1 × 2	2.686 (2)
Al—Si2 × 2	2.600 (1)	Al—Ge2 × 2	2.643 (2)
Li—Si1 × 2	2.666 (5)	Li—Ge1 × 2	2.70 (1)
Li—Si2 × 2	2.775 (5)	Li—Ge2 × 2	2.79 (1)

The application of the Zintl concept here [1] is more instructive than what we considered before on the examples of $Ca_2LiAlSi_2$ and $Ca_2LiAlGe_2$, given that no disorder is present and no assumptions need to be made. Hence, using the same scheme to partition the valence electrons, we can propose the following formulae breakdown: $(Sr^{2+})_2(Li^+)(4b\text{-}Al^{1-})(2b\text{-}Si^{2-})_2$ and $(Sr^{2+})_2(Li^+)(4b\text{-}Al^{1-})(2b\text{-}Ge^{2-})_2$. To arrive at these formulae, only Si—Al and Ge—Al interactions were treated as covalent. In a more extreme case, where Si—Li and Ge—Li bonds are also treated as covalent, all *Tt* atoms will be four-bonded and will bear no formal charge. Li with four covalent bonds must be considered formally as $4b\text{-}Li^{3-}$, in analogy with the Zintl clathrate $Ba_8Li_5Ge_{41}$ [11]. In this scenario, the valence electron count can be ascribed as follows: $(Sr^{2+})_2(4b\text{-}Li^{3-})(4b\text{-}Al^{1-})(4b\text{-}Si^0)_2$ and $(Sr^{2+})_2(4b\text{-}Li^{3-})(4b\text{-}Al^{1-})(4b\text{-}Ge^0)_2$.

The last remaining structure to briefly discuss is that of $Ba_2LiAlSi_2$ and $Ba_2LiAlGe_2$. The latter two compounds crystallize with the tetragonal space group $P4/nmm$ (no. 129). This is a structure type known as PbFCl (Pearson symbol *tP*6) [25], which is very common and well-known (Figure 4). There are three unique positions in the asymmetric unit (Table 4), meaning that Li and Al atoms are, again, statistically disordered.

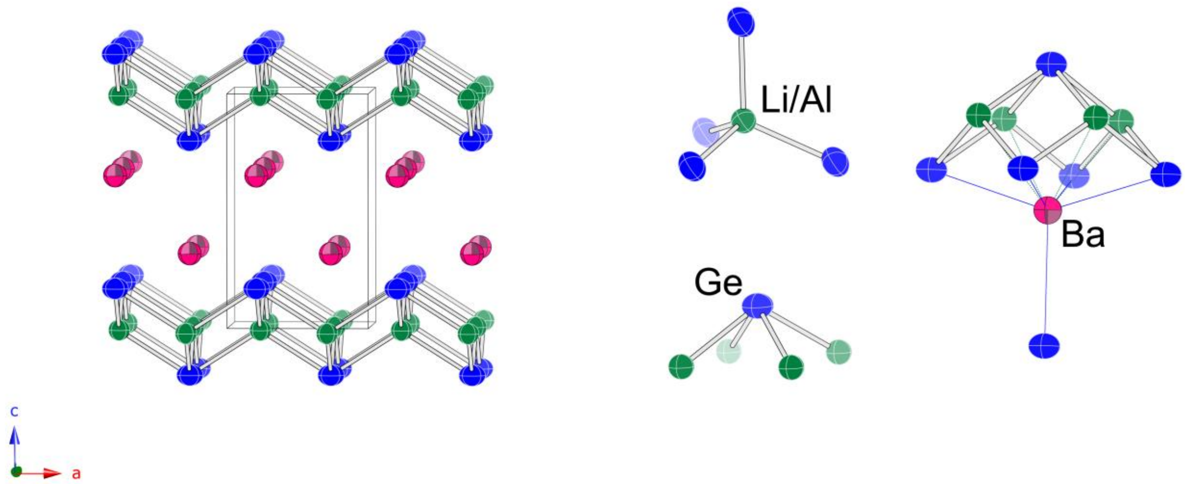

Figure 4. Schematic representation of the tetragonal crystal structure of $Ba_2LiAlGe_2$ (PbFCl structure type, space group $P4/nmm$). Green, blue, and magenta colors represent the Al/Li, Ge, and Ba atoms, respectively. Anisotropic displacement parameters are drawn at the 95% probability level.

From the schematic representation of the structure in Figure 4, it is evident that the overall arrangement of the atoms is nearly identical to that described above for the orthorhombic $Sr_2LiAlSi_2$ and $Sr_2LiAlGe_2$; the major difference is that the ordering of the tetrahedral $AlTt_4$ and $LiTt_4$ units is averaged in this symmetry. The Ba atoms take the space between the layers and have the exact same coordination environment (CN 9) as the Sr atoms in $Sr_2LiAlSi_2$ and $Sr_2LiAlGe_2$ (*vide supra*). Another Si atom is 3.9 Å away, i.e., is the topmost Si atom in Figure 4, for which a line denoting Si—Ba contact is not drawn.

Naturally, given that Ba is the largest element from group 2, all distances here are slightly longer compared to the Ca- and Sr-based compounds. Specifically, the average bond lengths of *A*–Al and *A*–Li (*A* = Ca, Sr, Ba) in $Ca_2LiAlTt_2$, $Sr_2LiAlTt_2$, and $Ba_2LiAlTt_2$ (*Tt* = Si, Ge) increase as the differing cation increases in size. In other words, the average *A*–Al and *A*–Li contacts in $Ca_2LiAlSi_2$ are shorter than those in $Sr_2LiAlSi_2$, which are in turn shorter than those in $Ba_2LiAlSi_2$. The same principle applies to the analogous germanides. For example, for the silicides, the average Ca–Al/Li distance is 3.14 Å, whereas the average Ba–Al/Li is 3.36 Å (recall that both structures have Al and Li atoms disordered).

Of note is also the fact that the fourfold symmetry in $Ba_2LiAlTt_2$ makes the tetrahedral units much closer to the ideal geometry, as they have four equal Li/Al–*Tt* bonds. Ge coordination environment is square pyramidal. All respective distances are tabulated in Table 7.

Table 7. Selected interatomic distances (Å) in $Ba_2LiAlSi_2$ and $Ba_2LiAlGe_2$.

$Ba_2LiAlSi_2$		$Ba_2LiAlGe_2$	
Atom Pair	**Distance/Å**	**Atom Pair**	**Distance/Å**
Ba—Li/Al × 4	3.3607 (5)	Ba—Li/Al × 4	3.3738 (7)
Ba—Si × 4	3.3812 (7)	Ba—Ge × 4	3.3974 (6)
Ba—Si	3.641 (2)	Ba—Ge	3.632 (2)
Si—Li/Al × 4	2.6992 (1)	Ge—Li/Al × 4	2.7340 (7)
Li/Al—Si × 4	2.6992 (1)	Li/Al—Ge × 4	2.7340 (7)

Just like with the cases of $Ca_2LiAlTt_2$ and $Sr_2LiAlTt_2$, in the fully ionic approximation, the structures of $Ba_2LiAlSi_2$ and $Ba_2LiAlGe_2$ can be rationalized as $(Ba^{2+})_2(Li^+)(Al^{3+})(Si^{4-})_2$ and $(Ba^{2+})_2(Li^+)(Al^{3+})(Ge^{4-})_2$.

4. Materials and Methods

4.1. Synthesis

Objective: To synthesize and establish the structure of a series of novel quaternary alkaline earth metal and rare earth metal silicides and germanides, with the base formula $A_2LiAlTt_2$ (A = Mg, Ca, Sr, Ba, Eu, Yb; Tt = Si, Ge). For this purpose, given that Li and most of the alkaline earth metals are reactive towards air and moisture, all synthetic and post-synthetic manipulations were performed inside an argon-filled glove box or under vacuum.

All metals were used as received from Alfa or Aldrich (>99.9% wt.), except for Ba and Li, whose surfaces had to be carefully cleaned with a blade each time the metal rods were cut. In a typical experiment, a mixture of elements with the desired stoichiometric ratio (total weight ca. 500 mg) was loaded into a Nb tube, which was then sealed by arc welding under an Ar atmosphere. The welded Nb tube was subsequently enclosed in a fused silica tube, which was flame-sealed under vacuum (below discharge).

To synthesize $A_2LiAlSi_2$ and $A_2LiAlGe_2$, the tubes with the reactant mixtures inside were heated in tube furnaces to 1223 K (rate of 300 K/h) and equilibrated for 8 h, followed by a cooling to 573 K at a rate of 200 K/h. The tubes were rotated in the furnaces at temperatures > 973 K. At the completion of their heat treatment, all tubes were quenched in cold water. The products of this method were not phase-pure.

Note: Many of the compounds detailed in this paper react rapidly with air and/or moisture. Corresponding with periodic trends, the germanides are more reactive than the silicide compounds. Moreover, the compounds' reactivity can be represented as $Ca_2LiAlTt_2$ < $Sr_2LiAlTt_2$ < $Ba_2LiAlTt_2$. $A_2LiAlGe_2$ (A = Ca, Sr, Ba) samples reacted with the ambient air and turned opaquely yellow within a few minutes. The $A_2LiAlSi_2$ samples experienced no visible color changes, but were not air stable beyond one hour, even when covered under an oil film. In direct contact with deionized water, both $A_2LiAlSi_2$ and $A_2LiAlGe_2$ ignited and volatilized. Due to these compounds' extreme sensitivity to the ambient atmosphere, further characterization besides the crystallographic work could not be effectively completed.

4.2. Crystallographic Studies

Powder X-ray diffraction (PXRD) measurements were carried out at room temperature on a Rigaku Miniflex diffractometer (filtered Cu $K\alpha$ radiation, λ = 1.5418 Å). Small portions of the obtained samples were ground into powder using agate mortars and pestles inside the argon-filled glovebox. The specimens for PXRD were prepared by covering the polycrystalline material with a light film of oil and were transferred to another glovebox, which housed the diffractometer. The data were collected as quickly as possible with a typical θ–θ scan of 0.05°/step and data acquisition rate of 2 s/step. The collected powder X-ray diffraction patterns were used for phase identification of the reaction products only.

The PXRD measurements before and after exposure to air over confirmed the previously stated instability in air.

Single-crystal X-ray diffraction data for the six compounds were collected at 200 K using a Bruker SMART CCD-based diffractometer (three-circle goniometer; monochromated Mo $K\alpha$ radiation (λ = 0.710 73 Å)). Firstly, several crystals from each batch were selected and checked before the best ones were chosen for intensity data collection. The experiments were managed in batch runs consisting of an appropriate number of frames to ensure 98+% coverage in angular range in 2θ of up to ca. 60° (frame width was typically 0.5–0.6° in ω and θ with a data acquisition rate of 6–8 s/frame). Data processing was performed with the Bruker supplied software. SADABS was used for semi-empirical absorption correction based on equivalents [48]. The structure factors were sorted and merged by the subprogram XPREP in the SHELXTL software package [49], which was also employed in the space group determination. The structures were solved by direct methods and refined to convergence by full-matrix least-squares methods on F^2. Selected details of the data collection and relevant crystallographic parameters are given in Tables 1–4. Refined distances are tabulated in Tables 5–7.

Author Contributions: Conceptualization, S.B.; methodology, P.K., L.C.P.-Q. and G.M.D.; data curation, P.K., L.C.P.-Q. and G.M.D.; validation, P.K., L.C.P.-Q., G.M.D. and S.B.; formal analysis, S.B.; investigation, P.K., L.C.P.-Q. and G.M.D.; resources, S.B.; writing—original draft preparation, P.K.; writing—conceptualization, P.K. and S.B.; writing—review and editing, S.B.; visualization, S.B.; supervision, S.B.; project administration, S.B.; funding acquisition, S.B. All authors have read and agreed to the published version of the manuscript.

Funding: This work was supported by the US National Science Foundation (NSF) through grant DMR-2004579.

Data Availability Statement: The corresponding crystallographic information files (CIF) have been deposited with the Cambridge Crystallographic Database Centre (CCDC) and can be obtained free of charge via http://www.ccdc.cam.ac.uk/conts/retrieving.html (or from the CCDC, 12 Union Road, Cambridge CB2 1EZ, UK; Fax: +44-1223-336033; E-mail: deposit@ccdc.cam.ac.uk) with the following depository numbers: 2285060–2285065.

Acknowledgments: The authors thank T.-S. You for early exploratory work in the Ca–Li–Al–Ge system and M. O. Ogunbunmi for help with single-crystal X-ray diffraction data. P.K. gives thanks to Jennifer Toner and Konstantinos Kontomaris for their exceptional guidance and encouragement throughout this project.

Conflicts of Interest: The authors declare no conflict of interest.

References

1. Nesper, R. The Zintl-Klemm Concept—A Historical Survey. *Z. Anorg. Allg. Chem.* **2014**, *640*, 2639–2648. [CrossRef]
2. Toberer, E.S.; May, A.F.; Snyder, G.J. Zintl Chemistry for Designing High Efficiency Thermoelectric Materials. *Chem. Mater.* **2010**, *22*, 624–634. [CrossRef]
3. Kauzlarich, S.M.; Brown, S.R.; Snyder, G.J. Zintl Phases for Thermoelectric Devices. *Dalton Trans.* **2007**, *21*, 2099. [CrossRef]
4. Yang, Z.; Trask, S.E.; Gilbert, J.A.; Li, X.; Tsai, Y.; Jansen, A.N.; Ingram, B.J.; Bloom, I. Exploring the Promise of Multifunctional "Zintl-Phase-Forming" Electrolytes for Si-Based Full Cells. *ACS Appl. Mater. Interfaces* **2022**, *14*, 53860–53871. [CrossRef]
5. McDowell, M.T.; Lee, S.W.; Nix, W.D.; Cui, Y. 25th Anniversary Article: Understanding the Lithiation of Silicon and Other Alloying Anodes for Lithium-Ion Batteries. *Adv. Mater.* **2013**, *25*, 4966–4985. [CrossRef] [PubMed]
6. Madsen, G.K.H. Automated Search for New Thermoelectric Materials: The Case of LiZnSb. *J. Am. Chem. Soc.* **2006**, *128*, 12140–12146. [CrossRef] [PubMed]
7. Kauzlarich, S.M. Special Issue: Advances in Zintl Phases. *Materials* **2019**, *12*, 2554. [CrossRef]
8. Snyder, G.J.; Toberer, E.S. Complex Thermoelectric Materials. *Nat. Mater.* **2008**, *7*, 105–114. [CrossRef]
9. Böhme, B.; Minella, C.B.; Thoss, F.; Lindemann, I.; Rosenburg, M.; Pistidda, C.; Møller, K.T.; Jensen, T.R.; Giebeler, L.; Baitinger, M.; et al. B1-Mobilstor: Materials for Sustainable Energy Storage Techniques—Lithium Containing Compounds for Hydrogen and Electrochemical Energy Storage. *Adv. Eng. Mater.* **2014**, *16*, 1189–1195. [CrossRef]
10. Shi, X.-L.; Zou, J.; Chen, Z.-G. Advanced Thermoelectric Design: From Materials and Structures to Devices. *Chem. Rev.* **2020**, *120*, 7399–7515. [CrossRef]
11. Nolas, G.S. *The Physics and Chemistry of Inorganic Clathrates*; Springer Science+Business Media: Dordrecht, The Netherlands, 2014.

12. Ghosh, K.; Ovchinnikov, A.; Baitinger, M.; Krnel, M.; Burkhardt, U.; Grin, Y.; Bobev, S. Lithium Metal Atoms Fill Vacancies in the Germanium Network of a Type-I Clathrate: Synthesis and Structural Characterization of $Ba_8Li_5Ge_{41}$. *Dalton Trans.* **2023**, *52*, 10310–10322. [CrossRef] [PubMed]
13. Dopilka, A.; Weller, J.M.; Ovchinnikov, A.; Childs, A.; Bobev, S.; Peng, X.; Chan, C.K. Structural Origin of Reversible Li Insertion in Guest-Free, Type-II Silicon Clathrates. *Adv. Energy Sustain. Res.* **2021**, *2*, 2000114. [CrossRef]
14. Dopilka, A.; Childs, A.; Ovchinnikov, A.; Zhao, R.; Bobev, S.; Peng, X.; Chan, C.K. Structural and Electrochemical Properties of Type VIII $Ba_8Ga_{16-\delta}Sn_{30+\delta}$ Clathrate ($\delta \approx 1$) during Lithiation. *ACS Appl. Mater. Interfaces* **2021**, *13*, 42564–42578. [CrossRef] [PubMed]
15. Dopilka, A.; Childs, A.; Bobev, S.; Chan, C.K. Electrochemical Lithium Alloying Behavior of Guest-Free Type II Silicon Clathrates. *J. Phys. Chem. C* **2021**, *125*, 19110–19118. [CrossRef]
16. Dopilka, A.; Childs, A.; Bobev, S.; Chan, C.K. Understanding the Amorphous Lithiation Pathway of the Type I Ba_8Ge_{43} Clathrate with Synchrotron X-ray Characterization. *Chem. Mater.* **2020**, *32*, 9444–9457. [CrossRef]
17. Tarnev, T.; Wilde, P.; Dopilka, A.; Schuhmann, W.; Chan, C.K.; Ventosa, E. Surface Properties of Battery Materials Elucidated Using Scanning Electrochemical Microscopy: The Case of Type I Silicon Clathrate. *ChemElectroChem* **2019**, *7*, 665–671. [CrossRef]
18. Wagner, N.A.; Raghavan, R.; Zhao, R.; Wei, Q.; Peng, X.; Chan, C.K. Electrochemical Cycling of Sodium-Filled Silicon Clathrate. *ChemElectroChem* **2013**, *1*, 347–353. [CrossRef]
19. Peng, X.; Wei, Q.; Li, Y.; Chan, C.K. First-Principles Study of Lithiation of Type I Ba-Doped Silicon Clathrates. *J. Phys. Chem. C* **2015**, *119*, 28247–28257. [CrossRef]
20. Dopilka, A.; Peng, X.; Chan, C.K. Ab Initio Investigation of Li and Na Migration in Guest-Free, Type I Clathrates. *J. Phys. Chem. C* **2019**, *123*, 22812–22822. [CrossRef]
21. Dopilka, A.; Zhao, R.; Weller, J.M.; Bobev, S.; Peng, X.; Chan, C.K. Experimental and Computational Study of the Lithiation of $Ba_8Al_yGe_{46-y}$ Based Type I Germanium Clathrates. *ACS Appl. Mater. Interfaces* **2018**, *10*, 37981–37993. [CrossRef]
22. Zhao, R.; Bobev, S.; Krishna, L.; Yang, T.; Weller, J.M.; Jing, H.; Chan, C.K. Anodes for Lithium-Ion Batteries Based on Type I Silicon Clathrate $Ba_8Al_{16}Si_{30}$—Role of Processing on Surface Properties and Electrochemical Behavior. *ACS Appl. Mater. Interfaces* **2017**, *9*, 41246–41257. [CrossRef] [PubMed]
23. Yang, J.; Tse, J.S. Silicon Clathrates as Anode Materials for Lithium Ion Batteries? *J. Mater. Chem. A* **2013**, *1*, 7782–7789. [CrossRef]
24. Li, Y.; Raghavan, R.; Wagner, N.; Davidowski, S.K.; Baggetto, L.; Zhao, R.; Cheng, Q.; Yarger, J.L.; Veith, G.M.; Ellis-Terrell, C.; et al. Type I Clathrates as Novel Silicon Anodes: An Electrochemical and Structural Investigation. *Adv. Sci.* **2015**, *2*, 1500057. [CrossRef] [PubMed]
25. Pearson, W.B. *Pearson's Handbook of Crystallographic Data for Intermetallic Phases*; American Society for Metals: Metals Park, OH, USA, 1985.
26. Pauling, L. *The Nature of the Chemical Bond*; Cornell University Press: Ithaca, NY, USA, 1960.
27. Wu, H.; Zhang, H.; Cheng, X.; Cai, L. Structure and Thermodynamic Properties of Li8Al3Si5. *J. Alloys Compd.* **2006**, *426*, 57–63. [CrossRef]
28. Kevorkov, D.; Gröbner, J.; Schmid-Fetzer, R. The Al–Li–Si System. 1. A New Structure Type $Li_8Al_3Si_5$ and the Ternary Solid-State Phase Equilibria. *J. Solid State Chem.* **2001**, *156*, 500–505. [CrossRef]
29. Zheng, C.; Hoffmann, R.; Nesper, R.; von Schnerring, H.-G. Site Preferences and Bond Length Differences in $CaAl_2Si_2$-Type Zintl Compounds. *J. Am. Chem. Soc.* **1986**, *108*, 1876–1884. [CrossRef]
30. Burdett, J.K.; Miller, G.J. Fragment Formalism in Main-Group Solids: Applications to Aluminum Boride (AlB_2), Calcium Aluminum Silicide ($CaAl_2Si_2$), Barium-Aluminum ($BaAl_4$), and Related Materials. *Chem. Mater.* **1990**, *2*, 12–26. [CrossRef]
31. Kauzlarich, S.M.; Condron, C.L.; Wassei, J.K.; Ikeda, T.; Snyder, G.J. Structure and High-Temperature Thermoelectric Properties of $SrAl_2Si_2$. *J. Solid State Chem.* **2009**, *182*, 240–245. [CrossRef]
32. Zevalkink, A.; Bobnar, M.; Schwarz, U.; Grin, Y. Making and Breaking Bonds in Superconducting $SrAl_{4-x}Si_x$ ($0 \leq x \leq 2$). *Chem. Mater.* **2017**, *29*, 1236–1244. [CrossRef]
33. Condron, C.L.; Hope, H.; Paula, P.M.B.; Schultz, A.J.; Kauzlarich, S.M. Synthesis, Structure, and Properties of $BaAl_2Si_2$. *Inorg. Chem.* **2007**, *46*, 4523–4529. [CrossRef]
34. Kranenberg, C.; Johrendt, D.; Mewis, A. Untersuchungen zum Existenzgebiet des $CaAl_2Si_2$-Strukturtyps bei ternären Siliciden. *Z. Anorg. Allg. Chem.* **1999**, *625*, 1787–1793. [CrossRef]
35. Kranenberg, C.; Mewis, A. Darstellung und Kristallstrukturen von $Ln_2Al_3Si_2$ and Ln_2AlSi_2 (*Ln*: Y, Tb–Lu). *Z. Anorg. Allg. Chem.* **2000**, *626*, 1448–1453. [CrossRef]
36. Condron, C.L.; Porter, R.; Guo, T.; Kauzlarich, S.M. Crystal Structures, Raman Spectroscopy, and Magnetic Properties of $Ba_{7.5}Al_{13}Si_{29}$ and $Eu_{0.27}Ba_{7.22}Al_{13}Si_{29}$. *Inorg. Chem.* **2005**, *44*, 9185–9191. [CrossRef] [PubMed]
37. Gulebaglan, S.E.; Dogan, E.K. Prediction the Structural, Electronic, Elastic and Dynamical Properties of LiAlGe and LiInGe Half-Heusler Crystals by Density Functional Theory. *Mater. Today Commun.* **2022**, *32*, 104082. [CrossRef]
38. Carrillo-Cabrera, W.; Gil, R.C.; Grin, Y. Refinement of the crystal structure of monocalcium dialuminide digermanide, $Ca[Al_2Ge_2]$. *Z. Krist. New Cryst. Struct.* **2001**, *216*, 535–536. [CrossRef]
39. Suen, N.-T.; Bobev, S. Structures of Three Alkaline-Earth Metal Germanides Refined from Single-Crystal X-ray Diffraction Data. *Chemistry* **2022**, *4*, 1429–1438. [CrossRef]

40. Kranenberg, C.; Johrendt, D.; Mewis, A. The Stability Range of the $CaAl_2Si_2$-Type Structure in Case of $Ln$$Al_2Ge_2$ Compounds. *Solid State Sci.* **2002**, *4*, 261–265. [CrossRef]
41. Leoni, S.; Carrillo-Cabrera, W.; Schnelle, W.; Grin, Y. $BaAl_2Ge_2$: Synthesis, Crystal Structure, Magnetic and Electronic Properties, Chemical Bonding, and Atomistic Model of the α↔β Phase Transition. *Solid State Sci.* **2003**, *5*, 139–148. [CrossRef]
42. Widera, A.; Eisenmann, B.; Schäfer, H.; Turban, K. Darstellung und Kristallstruktur von $Ca_3Al_2Ge_2$, $Sr_3Al_2Ge_2$ und $Ba_3Al_2Ge_2$/Preparation and Crystal S_tru_cture of $Ca_3Al_2Ge_2$, $Sr_3Al_2Ge_2$ and $Ba_3Al_2Ge_2$. *Z. Naturforsch B* **1976**, *31*, 1592–1595. [CrossRef]
43. Kranenberg, C.; Johrendt, D.; Mewis, A.; Pöttgen, R.; Kotzyba, G.; Rosenhahn, C.; Mosel, B.D. Structure and Properties of the Compounds $LnAl_2X_2$ (Ln = Eu, Yb; X = Si, Ge). *Solid State Sci.* **2000**, *2*, 215–222. [CrossRef]
44. Somer, M.; Carrillo-Cabrera, W.; Peters, E.M.; Peters, K.; von Schnering, H.G. Crystal structure of disodium lithium diphosphidoaluminate, Na_2LiAlP_2. *Z. Krist. Cryst. Mater.* **1995**, *210*, 778–779. [CrossRef]
45. Ovchinnikov, A.; Bobev, S. Zintl Phases with Group 15 Elements and the Transition Metals: A Brief Overview of Pnictides with Diverse and Complex Structures. *J. Solid State Chem.* **2019**, *270*, 346–359. [CrossRef]
46. Fernandes, R.M.; Coldea, A.I.; Ding, H.; Fisher, I.R.; Hirschfeld, P.J.; Kotliar, G. Iron Pnictides and Chalcogenides: A New Paradigm for Superconductivity. *Nature* **2022**, *601*, 35–44. [CrossRef] [PubMed]
47. Mizuguchi, Y.; Takano, Y. Superconductivity in PbO-Type Fe Chalcogenides. *Z. Krist.* **2011**, *226*, 417–434. [CrossRef]
48. *SADABS NT*, Version 2.10; Bruker Analytical X-ray Systems, Inc.: Madison, WI, USA, 2001.
49. *SHELXTL*, Version 6.12; Bruker Analytical X-ray Systems, Inc.: Madison, WI, USA, 2001.